Impact of helium neutral gas puff on plasma turbulence in linear magnetized argon plasmas

Impact of helium neutral gas puff on plasma turbulence in linear magnetized argon plasmas

T. Kobayashi[1,2], F. Kin[3], Y. Kawachi[4], M. Sasaki[5], Y. Kosuga[5], K. Yamasaki[5], and S. Inagaki[5]

[1] National Institute for Fusion Science, National Institutes of Natural Sciences, Toki 509-5292, Japan

[2] The Graduate University for Advanced Studies, SOKENDAI, Toki 509-5292, Japan

[3] National Institutes for Quantum and Radiological Science and Technology, Naka 311-0193, Japan

[4] Interdisciplinary Graduate School of Engineering Sciences, Kyushu University, Kasuga 816-8580, Japan

[5] Research Institute for Applied Mechanics, Kyushu University, Kasuga 816-8580, Japan

E-mail: kobayashi.tatsuya@nifs.ac.jp

Abstract. In order to explore the impact of the neutrals to the plasma turbulence, a new gas puff system is developed for a linear magnetized plasma column PANTA. Helium gas is injected to the argon plasma without changing the electron density profile. After the helium gas puff, the dominant fluctuation mode changes from the broadband $m = 2$ drift wave to the coherent $m = 1$ mode, where m is the azimuthal mode number. Accordingly, property of the nonlinear coupling with other fluctuating modes changes from broadband couplings to coherent couplings.

1. Introduction

Modeling of nonlinear turbulence dynamics in magnetically confined plasmas is acknowledged as one of the most attractive but challenging topics in basic and fusion plasma physics fields. In torus edge or scrape-off layer (SOL) plasmas, a certain amount of neutral particles remain un-ionized, which provides an additional degree of freedom for turbulence and flow dynamics. The SOL plasma properties determined by turbulent cross field transport significantly impact the core plasma performance through main-chamber recycling [1]. Cross field transport driven by convective cells in the SOL is found to be significantly affected by the local neutral density in basic torus plasmas [2, 3]. Radial electric field formation across the L-H transition is also influenced by the neutral density through the charge exchange damping force [4].

Neutral dynamics is also regarded as an important factor in drift wave systems in low temperature laboratory plasma columns, since the ionization fraction in those plasmas are often not very high. The ion-neutral collision is primarily considered to be a linear damping mechanism for the drift waves [5, 6] or the Kelvin Helmholtz instability [7]. However, nonlinear mesoscale fluctuating structures, such as zonal flows and streamers, formed in saturated drift wave turbulence system are found to vary according to the ion-neutral collision frequency or the neutral pressure [6, 8, 9, 10]. Nonlinear fluid simulation involving the neutral particle dynamics was recently implemented for calculating nonlinear turbulence evolution in the realistic experimental situation [11]. By taking into account the ionization process of neutrals in the ion fluid equation, a

new instability can be derived as well [12]. Turbulent Reynolds stress forces either in the azimuthal direction [13, 14, 15] or the parallel direction [16, 17] are eventually balanced by the neutral dragging force in steady state, therefore the neutral density profile significantly impacts the consequent flow structures. Blob propagation is shown to be possibly affected by the neutral wind in particular in linear magnetized plasma columns [18, 19]. Linear plasma research for simulating detached divertor plasmas is also an active field [20]. The neutral pressure is used as a control knob to displace the recombination front for the cross field transport study in the detached plasma [21].

In order to experimentally assess the impact of the neutrals on the turbulence and flow dynamics, neutral pressure scan experiments are occasionally performed in basic devices as one of the most simple operations [2, 9, 10, 14]. In the case of PANTA linear magnetized plasma, increasing the neutral pressure leads to not only increase of the neutral density but also concomitant growth of the electron density gradient [10]. Therefore, not only damping but also growth rate of the drift wave are simultaneously varied, which is unsuitable for interpretation of the background physics. A new control knob with which either the neutral density or the electron density gradient is solely changed is desirable.

In this paper, we report a newly installed helium gas puff system in the PANTA linear magnetized plasma device. The neutral helium gas is injected to the main argon plasma without changing the electron density gradient. After injecting the helium gas, the dominant turbulence structure decays and is overtaken by the subdominant mode

likely in response to the increased neutral density. Accordingly, property of the nonlinear coupling changes from broadband couplings to coherent couplings.

2. Experimental setup

Schematic of the PANTA system is shown in Fig. 1 (a). Cylindrical vacuum vessel with a length of 4050 mm and a diameter of 450 mm is surrounded by a set of magnetic coils having a capability to produce a homogeneous axial magnetic field in the range of $B = 0.04 - 0.15$ T. The argon neutral gas is fed from one side of the cylinder, which is ionized by a helicon wave at 3 kW and 7 MHz to produce a high density plasma [22]. The axial position z is defined as the axial distance from the edge of the vacuum vessel at the source region side. The 5 cm radius of the double loop helicon wave antenna determines the typical cylindrical plasma radius. Two annular baffles with an inner diameter of 15 cm are installed at both sides of the vessel for maintaining the neutral pressure constant in the plasma column [23]. In this study, the magnetic field strength and the neutral argon pressure are set to be 0.09 T and 0.5 mTorr, respectively. The ion-neutral collision frequency is a few tens of kilohertz. With this discharge condition, the streamer structure is nonlinearly excited by drift waves [24, 25, 26, 27]. In addition, drift waves also excite a sheared axial flow structure which secondarily drives the D'Angelo mode in the inner radii [16, 17].

The helium gas injector is illustrated in Fig. 1 (b), which is installed at the top side of the vacuum vessel at $z = 1125$ mm. High pressure helium gas (0.6 MPa) is filled in the

buffer tank having a volume of $\sim 0.56 \times 10^{-3}$ m^3, and injected to the vacuum vessel by opening the solenoid valve with a specific trigger signal. Since the first ionization energy of the helium atom is 1.56 times higher than the argon atom, the helium neutrals remain almost un-ionized in the argon plasma. The number of helium neutral particles injected per a single puff with 50 ms duration is estimated as 3×10^{19}. This is approximately the equivalent amount of the argon neutrals filled in the main vacuum vessel. The elastic collision cross-section for the ion-neutral collision in the low ion energy range is known to be proportional to the square root of the neutral polarizability divided by the ion thermal energy, i.e., the Langevin cross-section [28]. The polarizabilities of argon and helium are 1.64 Å^3 and 0.205 Å^3, respectively. Therefore, the ion-neutral collision frequency is accounted to be increased by 35.4 % by the 50 ms duration of the helium puff. The diffusion time of the helium gas in the axial direction is estimated as ~ 5 ms. Number of helium neutrals injected in a single puff can be controlled by changing the pulse duration.

In addition, the visible He I line emission is monitored at one of the side viewports at $z = 1125$ mm with a $f = 180$ mm and F/2.8 camera lens optics. The light is led to a 300 lines/mm grating spectrometer through optical fibers and detected by a charge coupled device (CCD) camera. The line emission intensity at 587.6 nm is used as an indicator of the helium neutral density [29].

Plasma turbulence fluctuation was diagnosed with electrostatic probe array systems. An azimuthal 64-channel probe array [30] is installed at $z = 1.875$ m. The

probe tips are made out of tungsten wire with a diameter of 0.8 mm and a length of 3 mm, and are aligned at a constant radius of $r = 4$ cm. The ion saturation current and the floating potential are alternately measured by the 64 tips, although only the ion saturation current fluctuation data are used in this study, as a proxy for density fluctuations. It should be noted that the density modulation plays a fundamental role in driving the streamer structure [31]. The radial distribution of the ion saturation current is measured with a radially scannable 5-channel radial rake probe installed at $z = 1.375$ m [32]. The radial rake probe has a spacing of $\Delta r = 1$ cm. In a series of two discharges with 0.5 cm radial displacement of the rake probe position, the radial range from $r = 2$ cm to $r = 6.5$ cm is measured with the radial resolution of $\Delta r = 0.5$ cm. All the probe signals are digitized with 1 MHz sampling analog-digital converters with an automatic data acquisition sequence system.

3. Experimental result

3.1. Helium injection sequence

Figure 2 shows the typical time evolution of one of the target discharges. The helium gas is injected in the middle of the discharge period at 0.3 s with the 50 ms duration as shown in Fig. 2 (a). The helium I intensity I_{HeI} quickly increases during the helium gas injection. Even after the helium gas injection is stopped, I_{HeI} remains high although it gradually decreases as time passes. This shows that the helium neutral density is maintained in the later discharge period. We define three different time periods for

discussing the evolution of the turbulence fluctuation property. Those are before the gas puff ($0.15 - 0.30$ s), after the gas puff ($0.35 - 0.50$ s), and during the gas puff ($0.30 - 0.35$ s). After the helium injection, spikes in the reflected power signal appear, which correspond to instant interruptions of the helicon discharge. The duration of those interruptions is typically 1–2 ms and the number of occurrences is less than 10. Total time duration that is contaminated by this interruptions is less than 10–20 ms, which is much shorter than the total averaging time duration of 150 ms. Therefore, discharge interruptions barely affect the spectral analysis presented below.

Time evolution of the windowed power spectrum density (PSD) of the normalized ion saturation current fluctuation at a tip of the 64-channel probe array is shown in Fig. 2 (b). Tukey window function with 5 ms duration is used. A coherent peak at $f \sim 4$ kHz is clearly enhanced by the helium gas puff, while high frequency broadband fluctuations at $f \sim 7 - 11$ kHz are suppressed. For quantitative discussion, the fluctuation power intensity is defined as the frequency integrated PSD, i.e.,

$$I_{f_1-f_2}(t) = \int_{f_2}^{f_1} P(t, f) df \tag{1}$$

where $P(t, f)$ is the windowed PSD and f_1 and f_2 are the frequency range of interest. Figure 2 (c) shows the time evolution of $I_{2.8-5.0\ \mathrm{kHz}}$ and $I_{5.4-13.0\ \mathrm{kHz}}$ as the mode energies of the low frequency coherent mode and the high frequency turbulence, respectively. The frequency ranges are heuristically determined to illustrate the overall picture of the fluctuation activity. Dominant fluctuation components are flipped by the helium gas puff. In addition, the total fluctuation power intensity below 50 kHz is amplified by

44 % after the helium gas puff.

Figure 3 presents spatial profiles of the mean value and the fluctuation power intensity in the ion saturation current signal before and after the helium gas puff. In the radial profile and the axial profile of the mean ion saturation current shown in Figs. 3 (a) and (b), no remarkable changes are exhibited. The injected helium gas is considered to remain un-ionized due to its higher ionization energy compared to the argon gas. It is confirmed that any detachment ionization front discussed in [21] is not formed in this case. For comparison, the case where the argon gas is injected instead of the helium gas by the same injector is discussed in the Appendix. As shown in Figs. 11 (a) and (b), both the radial profile and the axial profile show reasonable increments by the additional argon puff most likely because of its lower ionization energy.

Radial profiles of the fluctuation power intensities $I_{2.8-5.0\ \mathrm{kHz}}$ and $I_{5.4-13.0\ \mathrm{kHz}}$ are shown in Figs. 3 (c) and (d), respectively. The low frequency coherent mode intensity $I_{2.8-5.0\ \mathrm{kHz}}$ is amplified in the entire observed range of radius. The high frequency turbulence intensity $I_{5.4-13.0\ \mathrm{kHz}}$ has a pivot point at $r = 4.5$ cm, inside (outside) of which the fluctuation power intensity decreases (increases) after the helium gas puff.

3.2. Response in fluctuation spectrum

Fluctuating structures are resolved in detail by the two-dimensional Fourier analysis using data from the 64-channel probe array. Figures 4 (a) and (b) correspond to the frequency and mode number resolved PSD, here called the $f - m$ PSD, before and

after the helium gas puff. Here, the positive value of the mode number indicates the mode propagating in the electron diamagnetic drift direction. The $f - m$ PSD before the helium gas puff corresponds to the typical spectrum of the streamer. The mode at $(f, m) = (9.8\ \text{kHz}, 2)$ is considered to be the linearly unstable drift wave, according to the experimental fact that the density fluctuation and the potential fluctuation approximately satisfies the Boltzmann relation with a weak radially outward particle flux [33]. The mode at $(f, m) = (1.6\ \text{kHz}, -1)$ is the so-called mediator mode nonlinearly driven by the drift waves. The mediator mode back-reacts on the drift waves, and plays a role for broadening the drift wave spectrum [34, 31]. This broadening in the $f-m$ space is identical to the bunching of the fluctuation energy in the real space, which results in an azimuthally localized turbulent transport structure [27]. A dedicated comparison study of those experiments and a nonlinear fluid simulation also supports this interpretation [35]. Another coherent peak appears at $(f, m) = (4.2\ \text{kHz}, 1)$, having a narrower spectral shape and a higher spectral peak than the $m = 2$ drift wave. Note that the instability mechanism of the mode at $(f, m) = (4.2\ \text{kHz}, 1)$ is not identified. Fluctuation power intensities $I_{2.8-5.0\ \text{kHz}}$ and $I_{5.4-13.0\ \text{kHz}}$ in Fig. 2 and Fig. 3 correspond to the coherent $m = 1$ peak and broadened peaks around the $m = 2$ drift wave, respectively. As discussed above, the helium gas puff amplifies the coherent $m = 1$ mode and suppresses the broadband turbulence amplitude around the $m = 2$ drift wave.

In different discharges, the number of helium neutrals injected is scanned by controlling the pulse duration. By reducing the number of helium neutrals injected,

the changes in fluctuation spectra become less significant, but the main qualitative features are preserved.

To discuss the variation in the three-wave coupling process before and after the helium gas puff, two-dimensional auto-bicoherence with respect to the $m = -1$ mediator is calculated. The auto-bispectrum and the squared auto-bicoherence is defined as

$$B = \langle X_1 X_2 X_3^* \rangle \tag{2}$$

and

$$\hat{b}^2 = \frac{|B|^2}{\langle |X_1 X_2|^2 \rangle \langle |X_3|^2 \rangle}, \tag{3}$$

respectively, where $\langle\rangle$ indicates the ensemble average and $*$ denotes the complex conjugate. Two-dimensionally resolved Fourier component at (f_j, m_j) is expressed by X_j with j =1, 2, and 3. The biphase is given as the complex argument of the bispectrum, i.e.,

$$\phi_B = \tan^{-1} \frac{\mathrm{Im}[B]}{\mathrm{Re}[B]}. \tag{4}$$

where Re and Im denotes the real part and the imaginary part of a complex number. In the three-wave coupling process, the modes of interest must satisfy either one of two matching conditions, i.e., $(f_3, m_3) = (f_1, m_1) \pm (f_2, m_2)$. Figures 4 (c) and (d) show the squared auto-bicoherence as a function of (f_2, m_2), where (f_1, m_1) is fixed to the frequency and the mode number of the $m = -1$ mediator. The matching condition forces (f_3, m_3) to be $(f_1, m_1) + (f_2, m_2)$, where results with another matching condition $(f_1, m_1) - (f_2, m_2)$ are not shown here because of its qualitative similarity to the other.

Before the helium gas puff, the nonlinear coupling among the $m = -1$ mediator, the $m = 2$ drift wave, and its sidebands are prominent. Because of this nonlinear coupling processes, a diagonal broadening of the turbulent peaks occurs as a typical streamer formation mechanism. After the helium gas puff, this nonlinear coupling process is significantly weakened. Instead, the nonlinear coupling among the $m = -1$ mediator, the mode at $(f, m) = (4.2\ \text{kHz}, 1)$, and its sidebands becomes strong.

Figure 5 (a) represents slices of Figs. 4 (c) and (d) at $m = 1$ and 2 constant lines for specific frequency ranges. Corresponding plot for the biphase is shown as Fig. 5 (b). The helium gas puff attenuates the broadband nonlinear couplings with the $m = 2$ mode, and enhanced coherent peaks regarding $(f, m) = (4.2\ \text{kHz}, 1)$ mode only remain large after the gas puff. Changes in the biphase are generally less significant, implying that the nonlinear energy transfer directions are approximately maintained in each steady state. This does not apply in the transient phase of $0.30 - 0.35$ s, which will be shown below.

According to the nonlinear coupling analysis, we hypothesize that the fluctuation mode activities can be classified into two clusters: One is the $m = 2$ drift wave and its sidebands and another is the mode at $(f, m) = (4.2\ \text{kHz}, 1)$ and its sidebands. The former and the latter are called the high frequency (HF) cluster and the low frequency (LF) cluster, respectively, in the rest of this paper. The peak positions of the mediator, modes in the LF cluster, and modes in the HF cluster are shown by open circles, squares, and triangles in Figs. 4 (a) and (b), respectively. Interrelation among the modes in the

HF cluster and in the LF cluster as well as the $m = -1$ mediator is analyzed in the next part.

3.3. Interrelation among fluctuating modes

Here, we define fluctuation mode intensities for each peak in the $f - m$ PSD shown in Fig. 4. Figure 6 presents the frequency dependent $f - m$ PSD sliced at fixed mode numbers before and after the helium gas puff. Frequency ranges are defined for some of the spectral peaks so as to cover the frequency change due to the helium gas puff and to avoid a crosstalk with different peaks. These frequency ranges are determined by eye because some peaks are partially embedded in background fluctuations, which makes peak detection algorithms overly complicated for the purposes of this work. Defined frequency ranges are shown by colored rectangles and summarized in Table 1. The fluctuation power intensity is obtained by Eq. (1) for each peak. Figure 7 corresponds to the time evolution of the mode fluctuation power intensity for each spectral peak in a single discharge. Here, modes can be uniquely identified by the mode number and the belonging cluster. In addition to the evolution of the fluctuation power intensities across the helium gas puff, there also exist slow oscillations in quasi steady states before and after the helium gas puff.

To uncover the relation among the fluctuating modes, the cross correlation function is calculated for time periods before and after the helium gas puff as shown in Fig. 8. Here, the reference signal is set to be the $m = 1$ mode in the LF cluster. The auto-

correlation time of the fluctuation power intensity evolution is ~ 10 ms. In both of the time periods, the modes in the LF cluster have positive correlations with the $m = 1$ mode in the LF cluster. While, the modes in the HF cluster show anti-correlated behavior to the $m = 1$ mode in the LF cluster. The modes in different clusters are in a competing relation. It is speculated that the LF cluster modes and the HF cluster modes share a unique free energy source as the driving mechanism. The $m = -1$ mediator have a weak negative correlation with the modes in the HF cluster.

Because of the slow oscillations in the fluctuation power intensity evolution, it is difficult to discuss the relation of the modes across the helium gas puff in a single discharge, as shown in Fig. 7. To eliminate the oscillations that are independent of the transient response to the helium gas puff, 15 equivalent discharges are averaged. Relative change of the fluctuation power intensity with respect to the values before the helium gas puff is displayed in Fig. 9. Shaded regions around each curve represent the standard error in averaging. Fluctuation power intensities of the modes in the HF cluster quickly decay immediately after the helium gas puff is begun with almost no delay. The $m = -1$ mediator follows the evolution of the HF cluster modes. Growth of the modes in the LF cluster seem to occur with a finite delay of $10 - 20$ ms with respect to the helium injection time.

Transient responses in the squared auto-bicoherence and the biphase are shown in Fig. 10 for modes at $(f, m) = (4.2 \text{ kHz}, 1)$ and $(f, m) = (9.8 \text{ kHz}, 2)$ as representatives of modes in the LF cluster and the HF cluster, respectively. Ensemble averaging is

performed in a short time bins of 40 ms, where the window size of the short time Fourier transform is 5 ms. The horizontal errorbars in Fig. 10 correspond to the time bin width of 40 ms. This time averaging bin is longer than the period of the self-oscillation in the fluctuation power intensity of ~ 10 ms, as shown in Fig. 8. The time evolutions of the squared auto-bicoherence and the biphase are evaluated by shifting the time averaging bin with a 20 ms interval. To increase number of realizations, data form 15 independent discharges are also used. Before the gas puff, the squared auto-bicoherences show slight decreasing trends. Across the gas puff, the nonlinear coupling among modes in LF cluster and the mediator increases while that among modes in HF cluster and the mediator decreases. Those behaviors resemble the time evolutions of the fluctuation power intensity. The biphase among modes in LF cluster and the mediator meaningfully increases during the helium gas puff, and seems to slightly decrease back towards the original value once the gas puff is turned off. Change in the biphase among modes in HF cluster and the mediator is less significant than the former.

A possible interpretation of the dynamics is given as follows. First, the HF cluster modes that are in competition with the LF cluster modes are preferably attenuated by the helium injection. As a result, free energy that has been used by the HF cluster modes is released. The LF cluster modes are then allowed to grow by using that free energy, and the fluctuation system saturates to the new state.

Identification of the mode at $(f, m) = (4.2\ \mathrm{kHz}, 1)$ is a key to understanding the complicated dynamics discussed here. In linear devices, various instabilities including

Kelvin-Helmholtz modes, the centrifugal Rayleigh-Taylor modes, and D'Angelo modes were reported to be possibly excited in addition to resistive drift waves in experimental [16, 17, 36] and numerical [8, 37, 38] studies. Those instabilities can be candidates for the mode at $(f, m) = (4.2\ \mathrm{kHz}, 1)$, therefore we attempt to compare their characteristic features and observations. A key ingredient for mode examination is the axial wave structure obtained by the set of probes aligned in the axial direction at $r = 4$ cm. The axial mode number of the mode at $(f, m) = (4.2\ \mathrm{kHz}, 1)$ is $n = 0.1 - 0.2$, which is clearly smaller than that of the drift waves in HF cluster ($n \sim 1$) but is larger than that of the mediator ($n \sim 0$). Since the axial mode structure is not a flute-like, Kelvin-Helmholtz modes and the Rayleigh-Taylor modes can be excluded in general sense. Note that the PANTA plasma typically has an axial non-uniformity in the background density profile as shown in Fig. 3 (b). Impact of this axial profile non-uniformity on the flute structure is assessed in feature, which would provide more solid conclusion for this discussion. D'Angelo modes can also be excluded because it can be excited in the strong axial flow shear region typically in $r < 3$ cm [16, 17].

Different types of mode competition events were reported in previous studies. In experiment, mutual interactions between streamers and solitary waves [9], different types of streamers [26], drift wave eddies and zonal flows [39], and drift waves and D'Angelo modes [17] were found. In numerical simulation, dynamic competitions among zonal flows, streamers, and flute modes utilizing the ion-neutral collision frequency as a control parameter were investigated in detail [6, 8]. A bifurcation of the plasma flow

pattern was seen in the drift wave-D'Angelo mode system [37]. In addition, a linear fluid simulation revealing the impact of the ion-neutral collision not only on drift waves but also D'Angelo modes is now being investigated [40]. The present observation adds a new type of competition between different clusters of drift waves nonlinearly connected to each other.

4. Summary

In this study, we developed a new helium gas puff system in the linear magnetized plasma column PANTA to investigate the impact of the neutral pressure on the plasma turbulence without changing the electron density profile. After the helium gas puff, the dominant fluctuation mode changed from the $m = 2$ drift wave to the $m = 1$ mode, accompanying a qualitative change in the nonlinear coupling property from the broadband couplings to the coherent couplings.

Acknowledgments

We acknowledge useful discussions with D. Kato and H. Tanuma, and thank S. Sakakibara and A. Fujisawa for strong support. This work is partly supported by the Grant-in-Aid for Scientific Research of JSPS (15H02155 and 17K14898), the collaboration programs of RIAM of Kyushu University and Asada Science Foundation.

Data availability statement

The data that support the findings of this study are available from the corresponding author upon reasonable request.

Appendix

Here, the response of the plasma profile and the plasma turbulence to the argon gas puff instead of the helium gas puff using the same system are shown. Figures 11 (a) and (b) show the radial profile and the axial profile of the mean ion saturation current. Because the injected neutral argon is ionized due to its lower ionization energy, the profiles show reasonable increments by the additional argon puff. Figures 11 (c) and (d) are the $f-m$ PSD before and after the argon gas puff. The variation in the mean profile provides a remarkable change in the fluctuation spectrum. The $f-m$ PSD after the argon gas puff is qualitatively equivalent to that observed in a discharge with the higher neutral argon pressure at the plasma source region [26].

Reference

[1] B LaBombard, M V Umansky, R L Boivin, J A Goetz, J Hughes, B Lipschultz, D Mossessian, C S Pitcher, J L Terry, *et al* 2000 *Nucl. Fusion* **40** 2041

[2] N Katz, J Egedal, W Fox, A Le, and M Porkolab 2008 *Phys. Rev. Lett.* **101** 015003

[3] D A D'ippolito, J R Myra, and S J Zweben 2011 *Phys. Plasmas* **18** 060501

[4] S Kitajima, H Takahashi, Y Tanaka, H Utoh, M Sasao, M Takayama, K Nishimura, S Inagaki, and M Yokoyama 2006 *Nucl. Fusion* **46** 200

[5] G R Tynan, C Holland, J H Yu, A James, D Nishijima, M Shimada, and N Taheri 2006 *Plasma physics and controlled fusion* **48** S51

[6] N Kasuya, M Yagi, K Itoh, and S-I Itoh 2008 *Phys. Plasmas* **15** 052302

[7] D M Fisher, B N Rogers, G D Rossi, D S Guice, and T A Carter 2015 *Phys. Plasmas* **22** 092121

[8] M Sasaki, N Kasuya, K Itoh, M Yagi, and S-I Itoh 2014 *Nucl. Fusion* **54** 114009

[9] H Arakawa, S Inagaki, Y Nagashima, T Yamada, K Kamataki, T Kobayashi, S Sugita, M Yagi, N Kasuya, A Fujisawa, *et al* 2010 *Plasma Phys. Control. Fusion* **52** 105009

[10] T Kobayashi, S Inagaki, M Sasaki, Y Kosuga, H Arakawa, F Kin, T Yamada, Y Nagashima, N Kasuya, A Fujisawa, *et al* 2017 *Plasma Fusion Res.* **12** 1401019–1401019

[11] N Kasuya, S Abe, M Sasaki, S Inagaki, T Kobayashi, and M Yagi 2018 *Phys. Plasmas* **25** 012314

[12] A S Ware, P H Diamond, H Biglari, B A Carreras, L A Charlton, J-N Leboeuf, and A J Wootton 1992 *Physics of Fluids B: Plasma Physics* **4** 877–887

[13] C Holland, J H Yu, A James, D Nishijima, M Shimada, N Taheri, and G R Tynan 2006 *Phys. Rev. Lett.* **96** 195002

[14] B M Annaratone, A Escarguel, T Lefevre, C Rebont, N Claire, and F Doveil 2011 *Phys. Plasmas* **18** 032108

[15] S Chakraborty Thakur, M Xu, P Manz, N Fedorczak, C Holland, and G R Tynan 2013 *Phys. Plasmas* **20** 012304

[16] S Inagaki, T Kobayashi, Y Kosuga, S-I Itoh, T Mitsuzono, Y Nagashima, H Arakawa, T Yamada, Y Miwa, N Kasuya, *et al* 2016 *Sci. rep.* **6** 22189

[17] T Kobayashi, S Inagaki, Y Kosuga, M Sasaki, Y Nagashima, T Yamada, H Arakawa, N Kasuya, A Fujisawa, S-I Itoh, and K Itoh 2016 *Phys. Plasmas* **23** 102311

[18] S I Krasheninnikov and A I Smolyakov 2003 *Phys. Plasmas* **10** 3020–3021

[19] G N Kervalishvili, R Kleiber, R Schneider, B D Scott, O Grulke, and T Windisch 2008 *Contrib. Plasma Phys.* **48** 32–36

[20] N Ohno 2017 *Plasma Physics and Controlled Fusion* **59** 034007

[21] H Tanaka, K Takeyama, M Yoshikawa, S Kajita, N Ohno, and Y Hayashi 2018 *Plasma Physics and Controlled Fusion* **60** 075013

[22] S Shinohara, T Hada, T Motomura, K Tanaka, T Tanikawa, K Toki, Y Tanaka, and K P Shamrai 2009 *Phys. Plasmas* **16** 057104

[23] M Ignatenko, M Azumi, M Yagi, S Shinohara, S-I Itoh, and K Itoh 2007 *Jpn. J. Appl. Phys.* **46** 1680

[24] T Yamada, S-I Itoh, T Maruta, N Kasuya, Y Nagashima, S Shinohara, K Terasaka, M Yagi, S Inagaki, Y Kawai, *et al* 2008 *Nat. Phys.* **4** 721–725

[25] T Yamada, S-I Itoh, S Inagaki, Y Nagashima, N Kasuya, K Kamataki, H Arakawa, T Kobayashi, M Yagi, A Fujisawa, *et al* 2010 *Phys. Rev. Lett.* **105** 225002

[26] T Kobayashi, S Inagaki, S Oldenburüger, K Kawashima, N Ohyama, Y Tobimatsu, H Arakawa, M Sasaki, Y Nagashima, T Yamada, *et al* 2012 *Plasma Fusion Res.* **7** 2401054–2401054

[27] F Kin, A Fujisawa, K Itoh, Y Kosuga, M Sasaki, S Inagaki, Y Nagashima, T Yamada, N Kasuya, K Yamasaki, *et al* 2019 *Phys. Plasmas* **26** 042306

[28] E A Mason and E W McDaniel. *Transport properties of ions in gases.* Wiley, New York, 1988.

[29] J R Myra, D A D'Ippolito, D P Stotler, S J Zweben, B P LeBlanc, J E Menard, R J Maqueda, and J Boedo 2006 *Phys. Plasmas* **13** 092509

[30] T Yamada, Y Nagashima, S Inagaki, Y Kawai, M Yagi, S-I Itoh, T Maruta, S Shinohara,

K Terasaka, M Kawaguchi, *et al* 2007 *Rev. Sci. Instrum.* **78** 123501

[31] Y Kosuga and K Hasamada 2018 *Physics of Plasmas* **25**(10) 100701

[32] N Ohyama, A Fujisawa, S Inagaki, Y Nagashima, S Oldenbürger, T Kobayashi, K Kawashima, Y Tobimatsu, T Yamashita, S Yamada, *et al* 2012 *Plasma Fusion Res.* **7** 1201025–1201025

[33] F Kin, T Yamada, S Inagaki, Y Nagashima, H Arakawa, T Kobayashi, Y Miwa, N Kasuya, M Sasaki, Y Kosuga, *et al* 2016 *J. Phys. Soc. Jpn.* **85** 093501

[34] K Nozaki, T Taniuti, and K Watanabe 1979 *J. Phys. Soc. Jpn.* **46** 991–1001

[35] T Yamada, M Sasaki, N Kasuya, Y Nagashima, S Inagaki, T Kobayashi, M Yagi, A Fujisawa, S-I I, and K Itoh 2013 *Plasma Fusion Res.* **8** 2401022–2401022

[36] F Brochard, E Gravier, and G Bonhomme 2005 *Phys. Plasmas* **12** 062104

[37] M Sasaki, N Kasuya, K Itoh, S Toda, T Yamada, Y Kosuga, Y Nagashima, T Kobayashi, H Arakawa, K Yamasaki, *et al* 2017 *Phys. Plasmas* **24** 112103

[38] M Sasaki, Y Camenen, A Escarguel, S Inagaki, Naohiro Kasuya, K Itoh, and T Kobayashi 2019 *Phys. Plasmas* **26** 042305

[39] H Arakawa, S Inagaki, M Sasaki, Y Kosuga, T Kobayashi, N Kasuya, Y Nagashima, T Yamada, M Lesur, A Fujisawa, *et al* 2016 *Sci. Rep.* **6** 1–7

[40] M Sasaki, T Kobayashi, S Inagaki, N Kasuya, and Y Kosuga 2020 *submitted to Phys. Plasmas*

Table 1. List of fluctuating modes and their belonging cluster

Mode number	Range of frequency [kHz]	Cluster
-1	0.8–3.6	Mediator
0	4.8–8.0	LF cluster
1	2.8–5.0	LF cluster
2	0.8–3.0	LF cluster
1	9.0–14.0	HF cluster
2	5.4–13.0	HF cluster
3	4.0–9.8	HF cluster
4	2.0–10.0	HF cluster

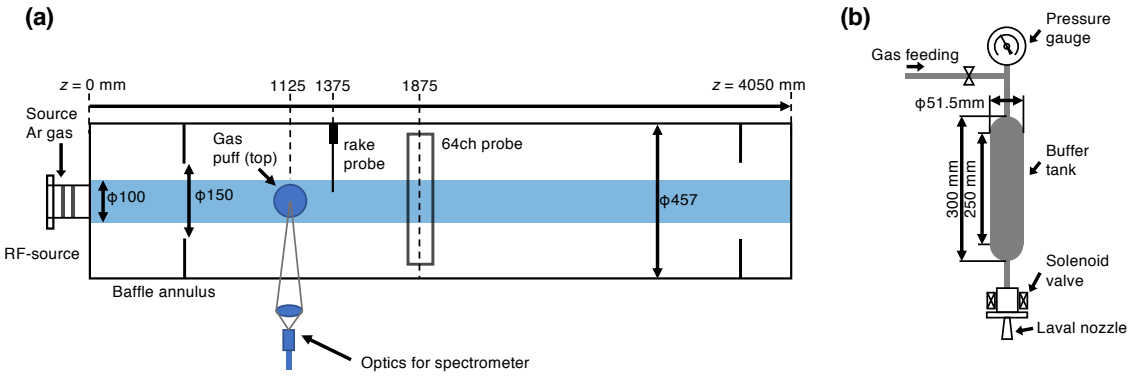

Figure 1. Schematics of (a) PANTA top view and (b) neutral gas puff system. Helium neutrals are injected to argon plasma aiming for perturbing the ion-neutral collision frequency by maintaining the electron density profile.

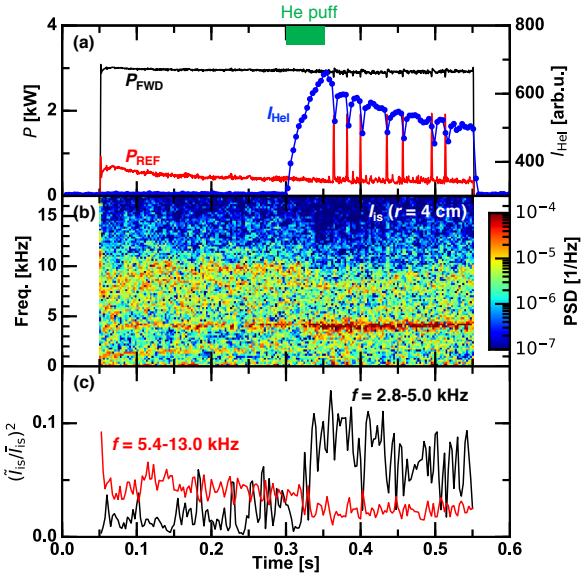

Figure 2. Time evolutions of (a) discharge scenario, (b) power spectral density of the ion saturation current fluctuation, and (c) fluctuation power intensities in particular ranges of the frequency. Helium gas injection time is indicated by the green rectangle on the top panel. By puffing helium neutrals dominant fluctuating mode switches from the higher frequency (5.2–13.0 kHz) broadband one to the lower frequency (2.8–5.0 kHz) coherent one.

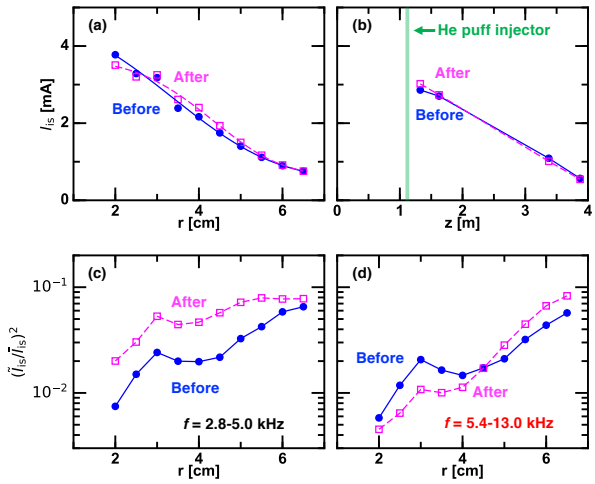

Figure 3. (a) Radial profile and (b) axial profile of the mean ion saturation current, and radial profiles of power intensities of the normalized ion saturation current fluctuation in (c) 2.8–5.0 kHz and (d) 5.2–13.0 kHz before and after the helium gas puff. The axial location of the helium puff injector is shown by thick green line in (b). Distributions of the fluctuation amplitude are significantly modified by the helium neutral puff, while mean profiles remain unchanged.

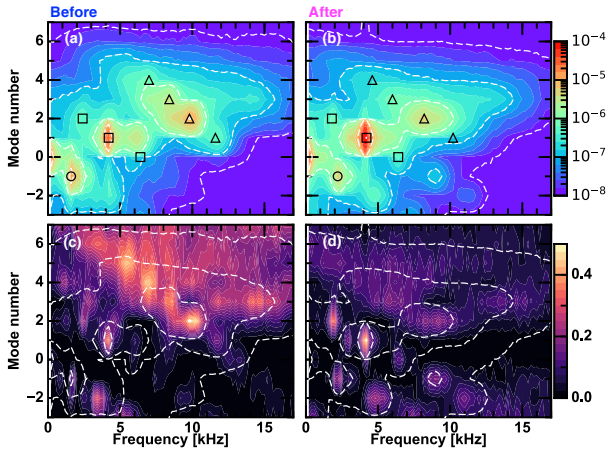

Figure 4. (a,b) Power spectral densities and (c,d) auto-bicoherences with respect to the $m = -1$ mediator of the normalized ion saturation current fluctuation resolved in the frequency-mode number space (a,c) before and (b,d) after the helium gas puff. Open circles, squares, and triangles in (a) and (b) show the peak positions of the mediator, modes in the LF cluster, and modes in the HF cluster, respectively. By the helium neutral puff, the dominant fluctuation mode changes from the broadband m = 2 drift wave to the coherent m = 1 mode being accompanied by the corresponding changes in the nonlinear couplings.

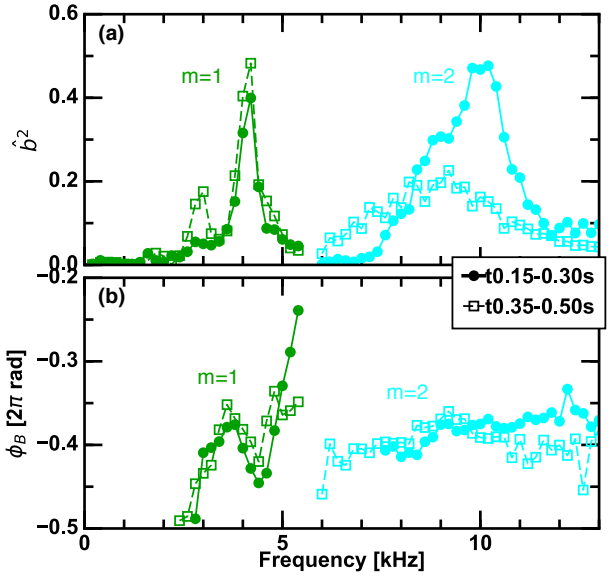

Figure 5. (a) Squared auto-bicoherence and (b) biphase as a function of the frequency for fluctuations at $m = 1, f \leq 5.4$ kHz and $m = 2, f \geq 6$ kHz. Curves correspond to the slices of Figs. 4 (c) and (d) at $m = 1$ and 2 constant lines. The nonlinear coupling strength in the m=2 broadband modes is attenuated by the helium neutral puff.

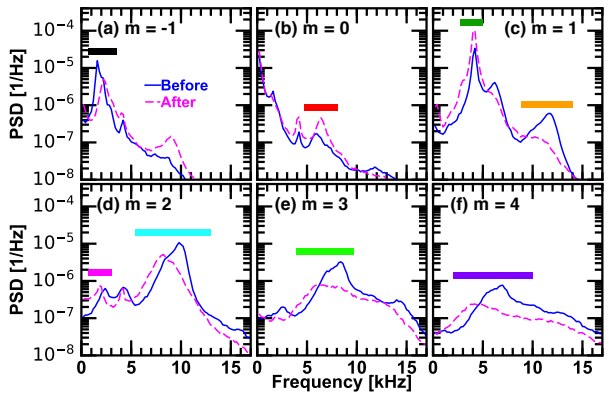

Figure 6. Frequency dependence of power spectral density for (a) $m = -1$, (b) $m = 0$, (c) $m = 1$, (d) $m = 2$, (e) $m = 3$, and (f) $m = 4$ before and after the helium gas puff. Colored rectangles correspond to the frequency integration ranges for mode power analysis. Both the frequency peaks and peak PSD values vary with the increased neutral density.

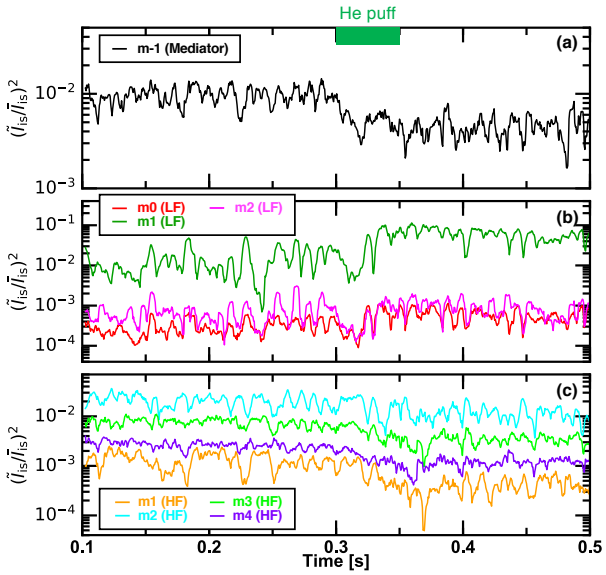

Figure 7. Time evolutions of fluctuation power intensities for spectral peaks (a) at the mediator, (b) in the LF cluster, and (c) in the HF cluster. Helium gas injection time is indicated by the green rectangle on the top panel. Slow oscillations in both steady states and transient evolution in response to the helium gas injection are shown.

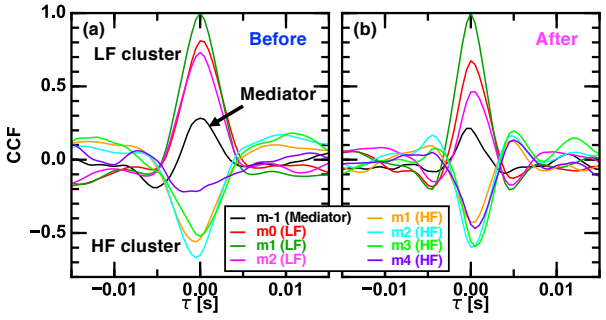

Figure 8. Cross correlation function of mode fluctuation power with respect to the $m = 1$ mode in the LF cluster (a) before and (b) after the helium gas puff. Modes in the LF cluster and those in the HF cluster compete each other.

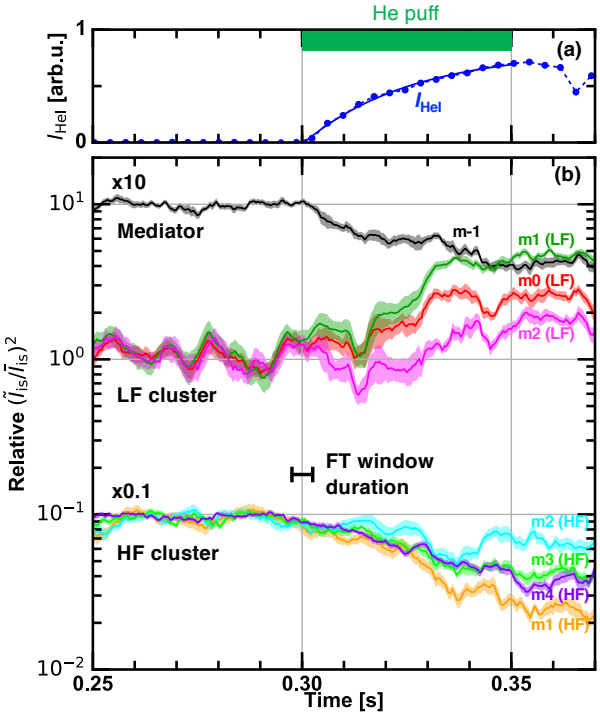

Figure 9. Time evolutions of (a) He I emission intensity and (b) relative fluctuation power with respect to the values before the helium gas puff. Helium gas injection time is indicated by the green rectangle on the top panel. Factors of $\times 10$ and $\times 0.1$ are applied for the mediator and modes in the HF cluster for vertically offsetting curves. Helium gas puff leads to suppressions in the HF cluster modes and the $m = -1$ mediator, while amplifies the LF cluster modes with a finite time delay of $10 - 20$ ms.

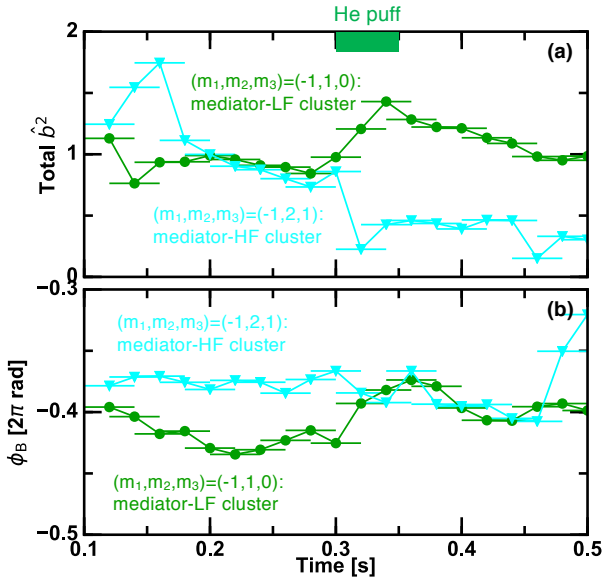

Figure 10. Time evolutions of (a) squared auto-bicoherence and (b) biphase for peaks at $(f, m) = (4.2\ \text{kHz}, 1)$ and $(f, m) = (9.8\ \text{kHz}, 2)$ in Fig. 4 (a), as representatives of modes in the LF cluster and the HF cluster, respectively. Helium gas injection time is indicated by the green rectangle on the top panel. Dynamics in squared auto-bicoherences resemble to those of the fluctuation power intensities. Biphase also evolves transiently during the helium gas puff.

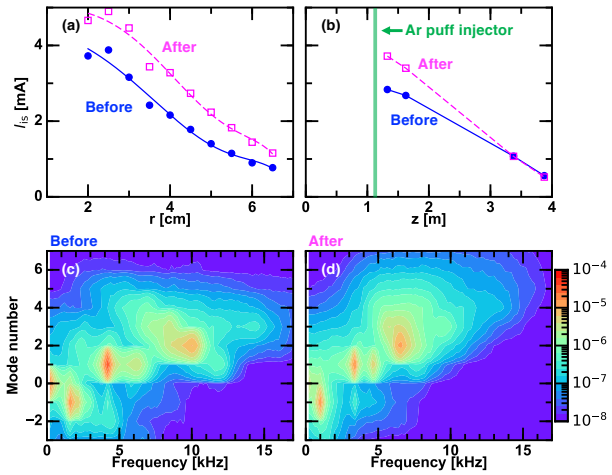

Figure 11. (a) Radial profile and (b) axial profile of the mean ion saturation current, and (c,d) power spectral densities of the normalized ion saturation current fluctuation resolved in the frequency and mode number space before and after the argon gas puff. The axial location of the helium puff injector is shown by thick green line in (b). Fluctuation spectrum after the argon puff is qualitatively equivalent to that observed in a discharge with the higher neutral argon pressure at the plasma source region.